Green Chemistry

PAPER

View Article Online
View Journal

Cite this: DOI: 10.1039/d5gc03726c

Electroenzymatic cascade synthesis of 2,3-diaminophenazine on HRP-$ZnGa_2O_4$ nano-biohybrids

Yuxuan Cheng,[a] Zhe Wang,[a] Siqi Li,[b] Meixuan Li,[a] Shuni Li,[a] Xue Xiao,*[b] Yucheng Jiang *[a] and Yu Chen [b]

In this work, a novel nano-biohybrid has been developed for the efficient synthesis of 2,3-diaminophenazine (DAP), a biologically significant heterocyclic compound, *via* an electroenzymatic cascade catalysis system. Horseradish peroxidase (HRP) was integrated with high-surface-area zinc gallate ($ZnGa_2O_4$) nanoflowers. The $ZnGa_2O_4$ component serves dual functions as an effective immobilization support for HRP and as an electrocatalyst for the two-electron oxygen reduction reaction (2e$^-$ORR) to generate hydrogen peroxide (H_2O_2) *in situ*. This *in situ* generated H_2O_2 directly activates the immobilized HRP, initiating the enzymatic oxidation of *o*-phenylenediamine (OPD) to DAP within the integrated nano-biohybrids. Capitalizing on nanoscale proximity, this architecture facilitates efficient channeling of H_2O_2 to the HRP active center and enables precise control over H_2O_2 yield through applied potential tuning, thereby matching enzymatic catalysis requirements. Consequently, this electroenzymatic cascade catalysis system achieves a 4.48-fold higher efficiency for DAP production compared to a conventional system relying on exogenous H_2O_2 addition, reaching 89.44% conversion of OPD in just 20 minutes. This work demonstrates the potential of coupling electrocatalysis and enzyme catalysis within integrated nano-biohybrids for developing highly efficient and controllable synthetic processes.

Received 20th July 2025,
Accepted 31st July 2025

DOI: 10.1039/d5gc03726c

rsc.li/greenchem

Green foundation

1. *Advancing green chemistry*: This work advances green chemistry by eliminating the need for hazardous bulk H_2O_2 (Principle #3) in DAP synthesis. We achieve this through a novel dual-functional $ZnGa_2O_4$ nanoflower biohybrid that generates and utilizes H_2O_2 *in situ* directly from oxygen and water using electrochemical activation.

2. *Specific green achievement*: Quantitatively: The system achieves significant process intensification (Principle #6), enabling 89.44% conversion to DAP in just 20 minutes – a 4.48-fold increase in synthesis efficiency compared to conventional methods requiring external H_2O_2. Qualitatively: The unique nanoflower architecture prevents waste (Principle #1) by enabling nanoscale channeling and immediate consumption of the electrogenerated H_2O_2. Precise potential control ensures a safe, on-demand reagent supply, inherently minimizing risks associated with H_2O_2 storage and transport.

3. *Greater sustainability*: The work's green foundation can be further improved by developing integrated membrane electrode assemblies (MEAs) to enhance scalability and energy efficiency.

Introduction

2,3-Diaminophenazine (DAP), a valuable phenazine derivative with unique electronic and biological properties, finds diverse applications in materials science, including use as an organic dye, a component of conductive polymers, and an energy storage material,[1–5] as well as in biotechnology, for instance, as a specific DNA-binding probe.[6–8] The significance of DAP as a synthetic intermediate underscores the demand for production methods that are both efficient and environmentally sustainable.[9–11] In this context, green chemistry principles, which prioritize renewable resources and waste minimization, provide a clear framework for moving beyond conventional syntheses that rely on hazardous solvents and harsh conditions.[12–15]

Enzymatic synthesis, characterized by high selectivity and mild operating conditions, aligns well with green chemistry goals.[13,16–18]Specifically, horseradish peroxidase (HRP) has been successfully applied in the oxidation reaction of *o*-phenylenediamine (OPD) to produce DAP.[19] However, a critical challenge lies in HRP's dependence on hydrogen peroxide

[a]*Key Laboratory of Macromolecular Science of Shaanxi Province, School of Chemistry and Chemical Engineering, Shaanxi Normal University, Xi'an, 710062, PR China. E-mail: jyc@snnu.edu.cn*

[b]*School of Materials Science and Engineering, Shaanxi Normal University, Xi'an, 710062, PR China. E-mail: xxiao@snnu.edu.cn*

(H_2O_2) for activating its heme group to form the crucial Compound **I** intermediate (P–Fe^{4+}=O). Excessive H_2O_2 would cause irreversible oxidative inactivation of the enzyme HRP,[20–23] necessitating precise control of H_2O_2. Conventional methods attempting to manage H_2O_2 concentrations, such as batch-wise addition of low H_2O_2 concentrations, suffer from significant drawbacks, including dilution effects, potential pH shifts, and greatly prolonged reaction times, ultimately failing to capitalize on the intrinsic efficiency of enzymatic catalysis and hindering large-scale application.[20]

To address these limitations, strategies integrating *in situ* H_2O_2 generation with enzymatic catalysis offer a compelling alternative.[21–24] Inspired by recent advances in electro- and photo-enzyme cascades,[25–28] we developed an integrated system that immobilizes HRP onto a nanostructure architecture designed for *in situ* electrocatalytic production of H_2O_2. Such an integrated H_2O_2-dependent enzymatic system provides some key advantages. First, H_2O_2 production can be precisely controlled by tuning the applied electrochemical potential, thereby matching enzymatic demand and preventing inactivation.[29–31] Second, overall cascade efficiency is enhanced through minimized H_2O_2 diffusion distances (due to nanoscale proximity) between the generation site and the HRP active center.[17,32,33] Finally, immobilization inherently improves the operational stability of HRP.

For the electrocatalytic component, the nano-flower structured zinc gallate ($ZnGa_2O_4$) was selected as a dual-function platform, serving as both the electrocatalyst for the two-electron oxygen reduction reaction (2e$^-$ORR) and the enzyme immobilization matrix.[34,35] $ZnGa_2O_4$ exhibits favorable selectivity for the 2e$^-$ORR pathway, while offering a high surface area due to its nano-flower structure, which is ideal for both effective electrocatalysis and robust enzyme loading – essential features for constructing an efficient nano-biohybrid.

Herein, we report the design and application of an HRP-immobilized $ZnGa_2O_4$ nanoflower nano-biohybrid (HRP-$ZnGa_2O_4$) for the efficient electroenzymatic synthesis of DAP from OPD. This system synergistically combines the potential-controlled electrocatalytic H_2O_2 generation capability of $ZnGa_2O_4$ with the oxidative power of HRP. Co-immobilization minimizes H_2O_2 diffusion distances, boosting cascade efficiency accordingly. Crucially, tuning the electrochemical potential allows the optimization of H_2O_2 generation kinetics to match enzymatic consumption, thereby maintaining optimal H_2O_2 levels and preventing inactivation of HRP. Compared to conventional methods relying on exogenous H_2O_2 addition, the HRP-$ZnGa_2O_4$ nano-biohybrid achieves a significantly enhanced DAP synthesis rate. This work highlights the potential of precisely regulated electroenzymatic cascade catalysis in nano-biohybrid architectures to advance green and sustainable chemical manufacturing.

Results and discussion

Characterization of $ZnGa_2O_4$

Nanoflower-like $ZnGa_2O_4$ was prepared by a solvothermal method. The X-ray powder diffraction (XRD) pattern confirms the formation of the pure spinel $ZnGa_2O_4$ phase (PDF#38-1240) with high crystallinity, evidenced by the well-defined diffraction peaks and the absence of impurity signals (Fig. 1a). The scanning electron microscopy (SEM) image reveals monodisperse nanoflowers with a uniform diameter of 4–5 μm, composed of self-assembled nanosheets (Fig. 1b and Fig. S1). The transmission electron microscopy (TEM) image further confirms this hierarchical structure, showing that the nanoflowers are assemblies of nanosheets (Fig. 1c). The high-resolution TEM (HRTEM) image exhibits clear lattice fringes (Fig. 1d), indicating the highly crystalline nature of the nanosheets. The measured lattice spacing of 0.24 nm corresponds to the (222) plane of spinel $ZnGa_2O_4$. The chemical composition and valence state of the $ZnGa_2O_4$ nanoflowers were characterized by energy-dispersive X-ray spectroscopy (EDX), X-ray photoelectron spectroscopy (XPS), and TEM mapping tests. The EDX data reveal that the $ZnGa_2O_4$ nanoflowers are mainly composed of elemental Ga, Zn, and O (Fig. 1e). The binding energies for Zn 2p, Ga 3d, and O1s are in excellent agreement with previously reported values for solvothermally synthesized $ZnGa_2O_4$.[36–38] The Zn 2p XPS spectrum displays the characteristic Zn $2p_{3/2}$ and Zn $2p_{1/3}$ peaks at 1021.1 eV and 1043.9 eV (Fig. 1f), indicative of Zn^{2+} in the spinel structure. The Ga 3d peak at 18.9 eV (Fig. 1g) is consistent with Ga^{3+}, and the O 1s peaks at 529.9 eV and 531.6 eV (Fig. 1h) correspond to lattice oxygen and oxygen vacancies, respectively. These results collectively confirm the presence of Zn^{2+}, Ga^{3+}, lattice oxygen, and oxygen vacancies within the $ZnGa_2O_4$ structure. Furthermore, TEM elemental mapping (Fig. 1i) demonstrates the homogeneous spatial distribution of Zn, Ga, and O throughout the nanoflower architecture. Such a uniform composition ensures consistent catalytic activity across the structure, underpinning the effective enzyme immobilization and efficiency in the 2e$^-$ORR.

Characterization of HRP-$ZnGa_2O_4$

The feasibility of HRP immobilization onto the $ZnGa_2O_4$ support was initially evaluated by measuring the zeta potential of $ZnGa_2O_4$ nanoflowers in phosphate buffer (PBS, pH 7.0), yielding a value of −21.8 mV (Fig. S2). This negative surface charge facilitates the effective binding of HRP primarily through electrostatic attraction, as HRP possesses positively charged surface residues (protonated amino groups) near neutral pH. Following immobilization, successful loading and a uniform distribution of HRP on $ZnGa_2O_4$ nanoflowers were confirmed through multiple characterization techniques. Confocal laser scanning microscopy (CLSM) of rhodamine B (Rh-B)-labeled HRP revealed that the superimposed bright-field and dark-field images showed excellent overlap (Fig. 2a), demonstrating the uniform immobilization of HRP across the $ZnGa_2O_4$ surface. TEM-elemental mapping of the HRP-$ZnGa_2O_4$ nano-biohybrids shows the presence of the elements Zn, Ga, C, N, O, Fe, and S (Fig. 2b). Critically, in contrast to bare $ZnGa_2O_4$, the HRP-$ZnGa_2O_4$ nano-biohybrid exhibited distinct N 1s and S 2p signals in its elemental maps (Fig. 2c–e and Fig. S3), which originate from the amino acid

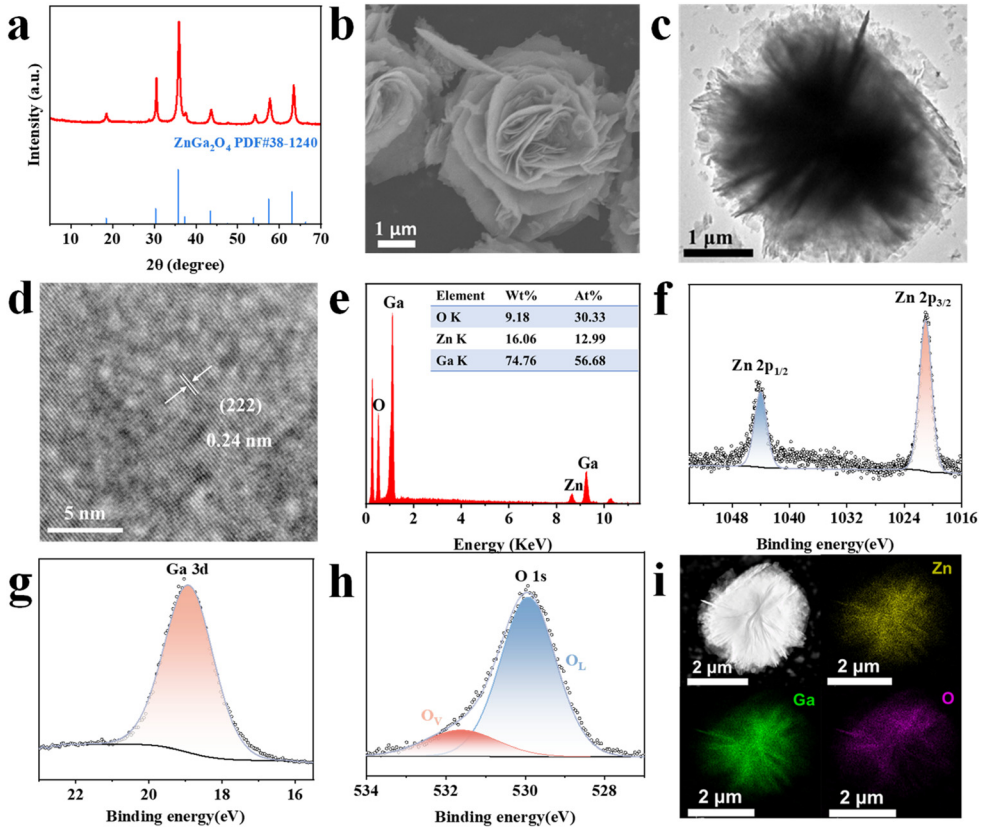

Fig. 1 (a) XRD pattern, (b) SEM image, (c) TEM image, (d) HRTEM image, (e) EDX pattern, (f) Zn 2p XPS spectrum, (g) Ga 3d XPS spectrum, (h) O 1s XPS spectrum, and (i) TEM-mapping images of $ZnGa_2O_4$ nanoflowers.

constituents of the HRP. The collective elemental mapping evidence, showing the co-localization of HRP-specific elements (C, N, S) with the $ZnGa_2O_4$ components (Zn, Ga, O), confirms the successful immobilization of HRP onto the support. The loading capacity of HRP on $ZnGa_2O_4$ was quantified as 19.57 mg g^{-1} (Fig. S4), which is attributed to the large specific surface area of the nanoflower morphology.

H_2O_2 generation on the nano-biohybrid

The selectivity of $ZnGa_2O_4$ for H_2O_2 generation *via* the ORR was investigated by a rotating ring-disk electrode (RRDE) test in O_2-saturated PBS at pH 7.0 (Fig. 3a). Analysis of the disk and ring currents within the potential window of 0.16 to −0.14 V yields an average electron transfer number (n) of approximately 2.36 and a corresponding H_2O_2 selectivity of 82.24% (Fig. 3b). These results demonstrate that $ZnGa_2O_4$ has excellent selectivity for the $2e^-$ORR. Moreover, the ORR activities of $ZnGa_2O_4$ and the HRP-$ZnGa_2O_4$ nano-biohybrid were determined and compared by linear scanning voltammetry (LSV) in PBS at pH 7.0. The LSV curves show that the ORR current density of HRP-$ZnGa_2O_4$ is only slightly smaller than that of bare $ZnGa_2O_4$ nanoflowers (Fig. 3c and d), possibly due to HRP blocking some of the active sites, in addition to the immobilized enzyme acting as a physical barrier that impedes the diffusion of dissolved oxygen.

The faradaic efficiency (FE) and yield of H_2O_2 during the $2e^-$ORR were quantified using the Ce^{4+} method (Fig. S5). Notably, while bare $ZnGa_2O_4$ exhibited the highest FE (99.44%) and an H_2O_2 yield of 14 μmol g^{-1} s^{-1} (Fig. 4a), the HRP-$ZnGa_2O_4$ nano-biohybrid showed a slightly lower FE (94.82%) but a significantly higher H_2O_2 yield of 47 μmol g^{-1} s^{-1} under identical conditions (Fig. 4b and c). This substantial enhancement in H_2O_2 yield suggests an additional electrocatalytic contribution from the immobilized HRP itself.

To elucidate the mechanism behind the enhanced $2e^-$ORR performance and higher H_2O_2 yield of HRP-$ZnGa_2O_4$, cyclic voltammetry (CV) was performed (Fig. 4d). The CV results of HRP-$ZnGa_2O_4$ displayed a well-defined redox couple at 0.29 V and 0.16 V *vs.* RHE, which was attributed to the Fe^{III}/Fe^{II} conversion within the heme group of HRP (eqn (1)).

$$\text{HRP-Fe}^{III} + H^+ + e^- \leftrightarrow \text{HRP-Fe}^{II} \quad (1)$$

In contrast, no such redox peaks were observed in the CV curves of bare $ZnGa_2O_4$. These well-defined redox peaks provide strong evidence for direct electron transfer (DET) between the immobilized HRP and the electrode surface, causing the conversion of iron species. Accordingly, this *in situ* generated Fe(II) facilitates the reduction of O_2 to H_2O_2.[39,40] The linear sweep voltammetry (LSV) of HRP in O_2-saturated PBS (Fig. S6) demonstrates significant ORR activity for HRP,

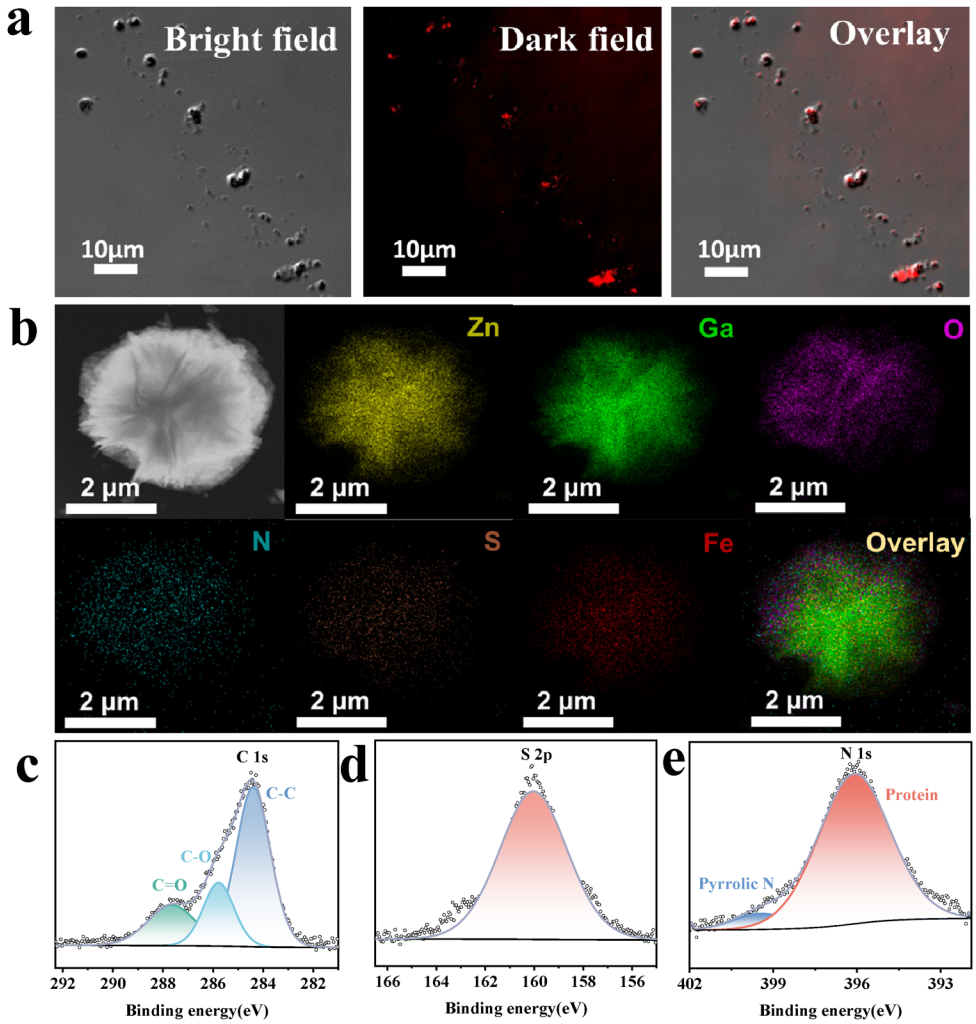

Fig. 2 (a) CLSM images, (b) TEM-mapping images, (c) C 1s XPS spectrum, (d) S 2p XPS spectrum, and (e) N 1s XPS spectrum of HRP-$ZnGa_2O_4$ nano-biohybrids.

further verifying HRP's ability to reduce O_2 electrocatalytically. The significantly higher H_2O_2 yield of the HRP-$ZnGa_2O_4$ compared to that of bare $ZnGa_2O_4$ (Fig. 4c) directly correlates with the DET-enabled generation of Fe^{II}.

The structure–property relationship for the HRP-$ZnGa_2O_4$

The catalytic activity of HRP is critically dependent on H_2O_2 concentration. While insufficient H_2O_2 limits the formation of catalytic intermediates, excess H_2O_2 leads to oxidative inactivation of the HRP.[41–43] Therefore, optimizing the ratio of $ZnGa_2O_4$ to HRP within the nano-biohybrid is essential to ensure that the electrochemically generated H_2O_2 concentration is optimal relative to the immobilized HRP content.

To address this crucial relationship, we systematically studied the impact of HRP loading on $ZnGa_2O_4$ on the overall cascade efficiency, while explicitly considering the influence of the applied potential, which affects the H_2O_2 generation. We first determined the optimal HRP loading on $ZnGa_2O_4$ to be 19.57 mg g^{-1}. The lower content of HRP than that of the $ZnGa_2O_4$ carrier implies that the instantaneous H_2O_2 flux generated *via* $ZnGa_2O_4$ electrocatalysis could readily exceed the capacity of the immobilized HRP, leading to enzyme deactivation and a reduction in the efficiency of the electroenzymatic cascade reaction. The catalytic efficiency of the cascade reaction increases significantly with higher HRP loading (Fig. 4e).

Fig. 4e also demonstrates that the applied potential can influence the catalytic efficiency of the cascade reaction (denoted by DAP production). It was found that at different potentials, the catalytic efficiency of the cascade reaction consistently enhanced with increasing HRP load efficiency. To maximize the overall cascade performance, we therefore conducted subsequent reactions using the maximum achievable HRP loading (19.57 mg g^{-1}) at the optimum applied potential of 0.16 V *vs.* RHE. This combination ensures sufficient H_2O_2 generation while minimizing the risk of HRP inactivation due to local H_2O_2 excess.

Reusability of the HRP-$ZnGa_2O_4$ nano-biohybrid

The unique 3D nanoflower morphology of $ZnGa_2O_4$ was hypothesized to provide a superior platform for HRP immobilization, offering both a high surface area and a protective

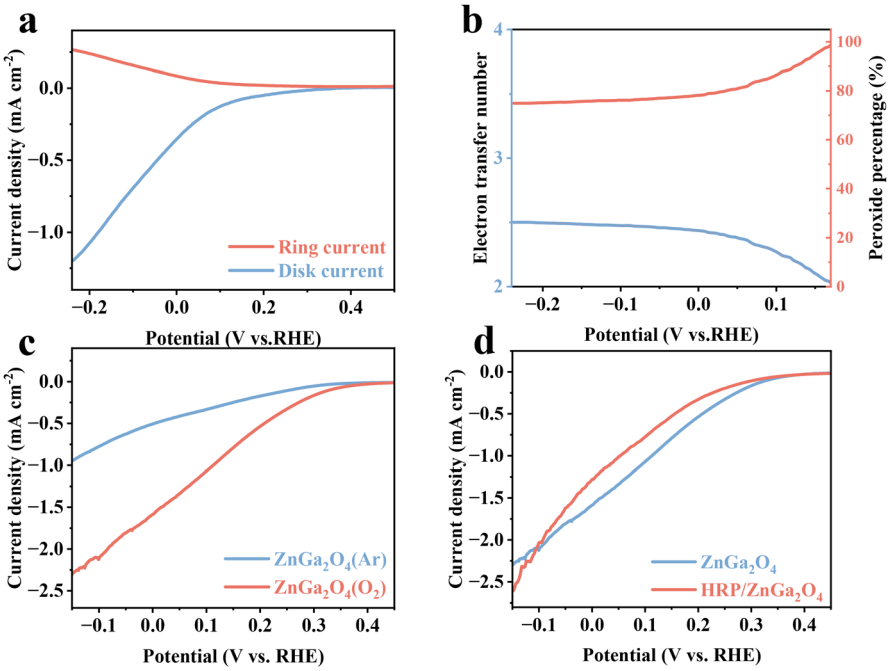

Fig. 3 (a) Rotating ring-disk electrode measurements for $ZnGa_2O_4$ at 1600 rpm in O_2-saturated 0.1 M PBS. (b) Electron transfer number and H_2O_2 selectivity of $ZnGa_2O_4$ at 1600 rpm in O_2-saturated 0.1 M PBS. (c) LSV curves of $ZnGa_2O_4$ in Ar or O_2-saturated PBS. (d) LSV curves of $ZnGa_2O_4$ and the HRP-$ZnGa_2O_4$ in O_2-saturated PBS.

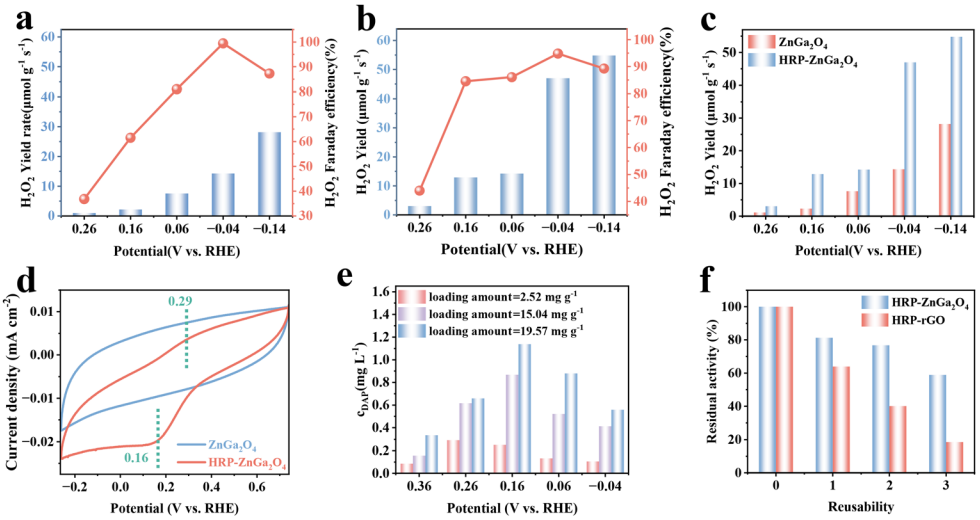

Fig. 4 (a) The yield of H_2O_2 and H_2O_2 Faraday efficiency of the ORR on $ZnGa_2O_4$ at different potentials, (b) the yield of H_2O_2 and H_2O_2 Faraday efficiency of the ORR on HRP-$ZnGa_2O_4$ at different potentials, (c) the yield of H_2O_2 of the ORR on $ZnGa_2O_4$ and HRP-$ZnGa_2O_4$ at different potentials, (d) the CV curve of $ZnGa_2O_4$ and HRP-$ZnGa_2O_4$ in N_2-saturated 0.1 M PBS, (e) DAP concentrations at different potentials for different loading amounts of $ZnGa_2O_4$ to HRP, and (f) comparison of reusability of the immobilized HRP on $ZnGa_2O_4$ and rGO, respectively.

microenvironment to enhance HRP stability. To test this hypothesis, the operational reusability of the HRP-$ZnGa_2O_4$ nano-biohybrid was evaluated by the residual activity (expressed by DAP yield), normalized to the initial (first cycle) activity (Fig. 4f). For comparison, a control biohybrid using reduced graphene oxide (HRP-rGO) was prepared, where rGO was selected because it is a well-established 2D platform that also performs the dual functions of 2e$^-$ORR electrocatalysis and enzyme immobilization. After three catalytic cycles, the HRP-$ZnGa_2O_4$ hybrid retained 59% of its initial activity, significantly higher than the 18% retention observed for HRP-rGO. These results validate that the unique morphology of the $ZnGa_2O_4$ support matrix is the key factor in enhancing HRP reusability within this integrated electroenzymatic cascade system.

Oxidation of OPD *via* the electroenzymatic cascade catalysis

The oxidation of OPD to DAP at the HRP-$ZnGa_2O_4$ nano-biohybrid *via* the electro-enzymatic cascade was monitored using UV-vis spectroscopy. This technique allows tracking of the reaction progress by observing the decrease in characteristic OPD absorbance peaks (at 234 nm and 282 nm) and the corresponding increase in DAP absorbance (peaks at 259 nm and 420 nm), illustrating the reactant-to-product conversion over time (Fig. S7). The UV-vis absorption spectra (Fig. 5a) display the background-corrected UV-vis absorption spectrum of DAP formed by electro-enzyme cascade catalysis of HRP-$ZnGa_2O_4$, revealing two well-defined characteristic peaks at 259 nm and 420 nm. These wavelengths are consistent with the positions of the DAP absorption peaks reported in the literature, confirming that the product is DAP.[19]

To further verify the advantages of the electro-enzyme cascade catalysis system, we applied it in the oxidation of OPD (5 mg L^{-1}) to DAP. The results show that the characteristic absorption of DAP by the electro-enzyme cascade catalysis was significantly higher than that by manual addition of H_2O_2 (Fig. 5b). This enhancement can be attributed to the nanoscale proximity effect between HRP and $ZnGa_2O_4$. The diffusion distance of the intermediate (H_2O_2) can be made shorter by co-immobilization of HRP with $ZnGa_2O_4$ on the same electrode. Meanwhile, the generated H_2O_2 is prohibited from diffusing into the bulk of the solution to improve the overall cascade efficiency. In addition, the conversion of OPD can reach 89.44% after 20 min of reaction *via* the electroenzymatic cascade catalysis of the HRP-$ZnGa_2O_4$ nano-biohybrid (Fig. 5c).

Proton and carbon NMR spectra were used to characterize the product further. The ^{1}H NMR chemical shifts of the oxidation product of OPD were δH1 = 6.23 (m, 4H), δH2 = 6.90 (m, 2H), δH3 = 7.51–7.57 (m, 2H), δH4 = 7.85–7.91 (m, 2H), and the integration ratio was δH4 : δH3 : δH2 : δH1 = 1 : 1 : 1 : 2, which gave the number of hydrogen atoms as 10, which is consistent with the number of hydrogen atoms in DAP (Fig. S8). In addition, the chemical shifts of the ^{13}C NMR spectra of the OPD oxidation products δ1 = 102.18, δ2 = 126.38, δ3 = 127.86, δ4 = 140.29, δ5 = 142.03, and δ6 = 144.02 confirm that the major product is DAP (Fig. S9).

The stability tests show a gradual increase in current density, after which the system stabilizes and remains within acceptable operational limits (Fig. S10). Crucially, the structural integrity of the HRP-$ZnGa_2O_4$ was maintained after stability testing. The flower-like morphology of the HRP-$ZnGa_2O_4$ catalyst on the cathode surface was retained (Fig. S11), and XRD showed that the catalyst was still $ZnGa_2O_4$ (Fig. S12), indicating good stability under the operating conditions.

Comparative analysis of recent DAP synthesis methodologies revealed that our phosphate buffer-based approach offers several significant advantages (Table 1): (1) the aqueous system eliminates organic solvent-associated toxicity, enhancing environmental sustainability; (2) the electroenzymatic cascade system enables controlled *in situ* H_2O_2 generation, preventing localized concentration spikes of reactive oxygen species; and (3) the enzyme immobilization strategy substantially improves catalyst recoverability and operational stability relative to free enzyme systems, establishing a foundation for bio-compatible catalytic system design.

Mechanism of oxidation of OPD

The electro-enzymatic cascade synthesis of DPA at the HRP-$ZnGa_2O_4$ nano-biohybrid is assumed to proceed as follows (Scheme 1). The process starts with the selective electrochemical generation of H_2O_2 *in situ via* the 2e$^-$ORR catalyzed by the $ZnGa_2O_4$ component at the applied potential. The resulting H_2O_2 then readily diffuses into the co-immobilized HRP and activates the enzyme's resting state (Fe^{III}). The activation begins with the heterolytic cleavage of the H_2O_2 molecule, which is a process that requires the transfer of two electrons from heme: one electron from Fe^{III} in the static HRP and the other from the porphyrin in the heme cofactor, generating a high iron porphyrin radical cation [[Fe(IV)O$^{\bullet}$]$^+$] (compound **I**). Compound **I** is a typical intermediate in HRP-catalyzed reactions, and is extremely unstable and highly oxidative. Compound **I** reacts with the electron-donating molecule OPD to form another intermediate oxidation state, compound **II**, and a radical of OPD. Compound **II** then reacts with OPD to form HRP and a radical of OPD.[55] The OPD radical then loses electrons to form the intermediate product *o*-quinonediimine. After that, in the presence of HRP and H_2O_2, compound **I** and compound **II** react with *o*-quinonediimine to form the *o*-quinonediimine radical, and the *o*-quinonediimine radical reacts with an OPD molecule to form the final product, DAP. In this

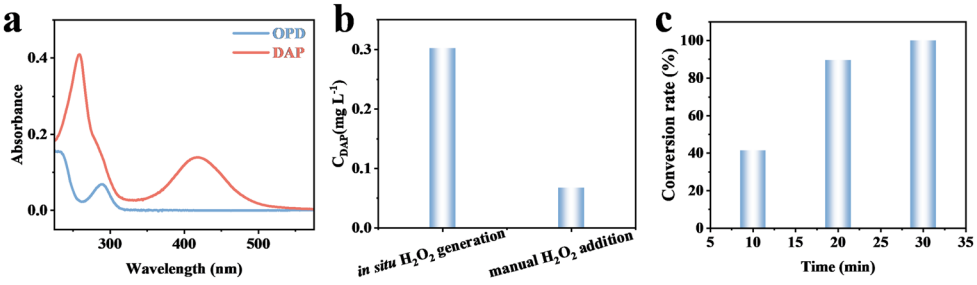

Fig. 5 (a) UV-vis absorption spectra of ODP and DAP. (b) DAP production concentrations: *in situ* H_2O_2 generation at −0.7 V and manual H_2O_2 addition. (c) Conversion rate of OPD to DAP at different reaction times.

Table 1 Comparison table for the synthesis of DAP using different catalysts

Catalyst	Temperature	Solvent	H_2O_2 generation method	Yield	References
HRP-$ZnGa_2O_4$	Room temperature	0.1 M phosphate buffered solution	*In situ* generation	62.5%	This work
FeTSPC	30 °C	0.2 M Na_2HPO_4-citric acid buffer	Manual addition	NA	2003[44]
Methemoglobin	Room temperature	0.1 M citrate-phosphate buffer	Manual addition	39%	2005[45]
Copper chloride dihydrate	Room temperature	Methanol	—	8.4%	2012[46]
$[Fe(L)Cl_2]Cl$	Room temperature	Methanol	Manual addition	NA	2015[47]
$[Fe(L)(NO_3)_2]NO_3$	Room temperature	Methanol	Manual addition	NA	2015[47]
$[Cu(L)(NO_3)_2]$	Room temperature	Methanol	—	NA	2015[48]
$[Cu(L)Br_2]$	Room temperature	Methanol	—	NA	2015[48]
Pd–Rh nanoframes and nanoboxes	Room temperature	Water	Manual addition	NA	2015[49]
$UO_2(NO_3)_2$	80 °C	Water	—	60%	2016[50]
Fe_3O_4@SiO_2-Cu	Room temperature	Water	Manual addition	NA	2017[51]
$MnFe_2O_4$	Room temperature	0.1 M citrate-phosphate buffer	Manual addition	NA	2018[52]
AgNPs/FP	Room temperature	Citrate-phosphate buffer	Manual addition	NA	2023[53]
$FeSnO(OH)_5$	100 °C	Water	Manual addition	43%	2024[54]

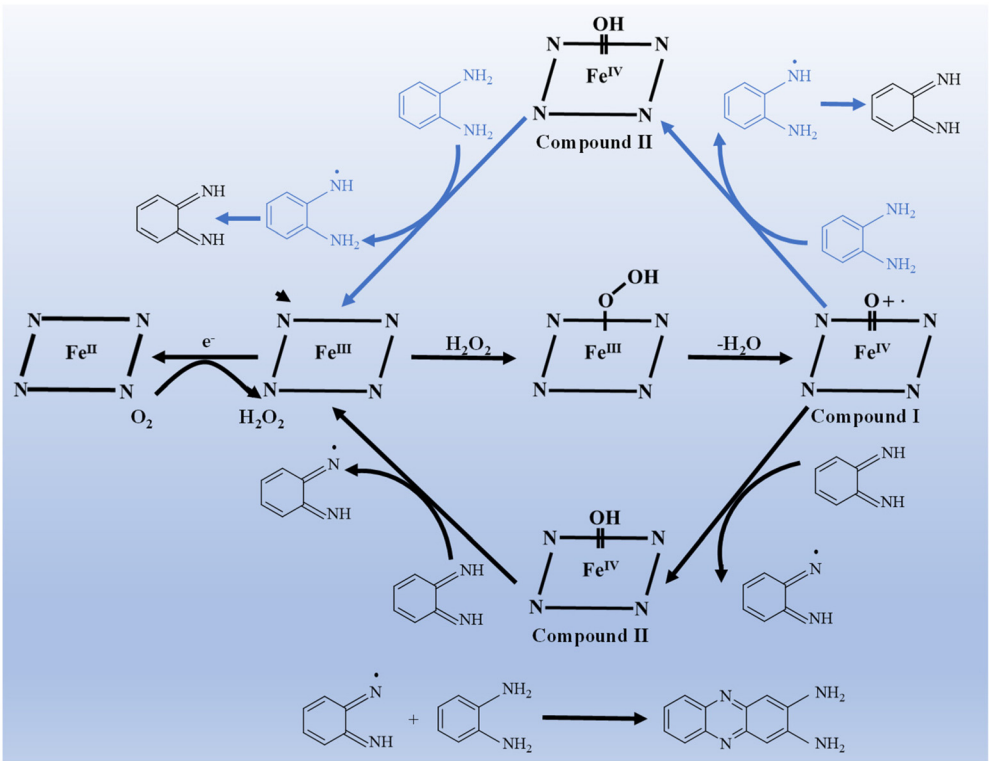

Scheme 1 Catalytic mechanism for the oxidation of OPD to DAP at the HRP-$ZnGa_2O_4$ nano-biohybrid *via* electroenzymatic cascade catalysis.

process, HRP and $ZnGa_2O_4$ were jointly involved in the electroenzymatic cascade catalysis, which facilitated the efficient proceeding of the above steps and ensured the successful synthesis of the final product DAP.[56] In addition, the DET-enabled generation of Fe^{II} contributes to the production of H_2O_2.

Conclusions

In summary, we engineered an integrated HRP-$ZnGa_2O_4$ nano-biohybrid supported on carbon cloth. The integrated system addressed critical green chemistry challenges by eliminating the need for hazardous, externally supplied H_2O_2 through *in situ* electrochemical generation from O_2 and H_2O. Critically, the unique 3D nanoflower architecture of $ZnGa_2O_4$ serves dual functions: catalyzing selective 2e⁻ORR to produce H_2O_2 while providing a protective microenvironment for immobilized HRP. This spatial design enables direct intermediate channeling, effectively eliminating diffusive H_2O_2 loss into the bulk solution and maximizing atom economy in the synthesis of DAP from OPD. The HRP-$ZnGa_2O_4$ demonstrated exceptional operational stability, retaining 59% of its initial activity after three reuse cycles—a substantial improvement over conventional 2D supports such as reduced graphene oxide (18% retention). Such enhanced re-

usability sharply reduces enzyme consumption and aligns with key principles of sustainable process design. The system operates continuously without external H_2O_2 addition, eliminating safety hazards associated with concentrated peroxide handling and reducing the environmental footprint of oxidative syntheses. Overall, this work highlights the strength of merging electrocatalysis and enzymatic catalysis in a thoughtfully designed nano-biohybrid framework, paving the way for advanced biocatalytic systems in sustainable synthesis.

Author contributions

Yuxuan Cheng: data curation, investigation, methodology, software, visualization, and writing – original draft. Zhe Wang: investigation, validation, visualization. Siqi Li: investigation, validation, and visualization. Meixuan Li: investigation, validation, and visualization. Shuni Li: methodology and supervision. Xue Xiao: supervision, methodology, formal analysis, resources, conceptualization, and writing – review & editing. Yucheng Jiang: supervision, methodology, formal analysis, resources, conceptualization, and writing – review & editing. Yu Chen: methodology, formal analysis, conceptualization, and writing – review & editing.

Conflicts of interest

There are no conflicts to declare.

Data availability

The data supporting the findings of this study are available within the article and its SI.

The SI includes experimental sections (synthesis, characterization, and electrochemistry) and additional figures. See DOI: **https://doi.org/10.1039/d5gc03726c**.

Acknowledgements

This work was supported by the National Natural Science Foundation of China (22273056), the Shaanxi Province Postdoctoral Science Foundation (2024BSHSDZZ080), the China Postdoctoral Science Foundation (2025M770156), and the Fundamental Research Funds for the Central Universities (GK202506037).

References

1 J. Liang, M. Tang, L. Cheng, Q. Zhu, R. Ji, X. Liu, Q. Zhang, H. Wang and Z. Liu, *J. Colloid Interface Sci.*, 2022, **607**, 1262–1268.
2 P. Qiu, Y. Li, H. Wang, D. Li, S. Wang and J. Yu, *Chem. Commun.*, 2022, **58**, 8982–8985.
3 W. Wang, S. Zhang, L. Zhang, R. Wang, Q. Ma, H. Li, J. Hao, T. Zhou, J. Mao and C. Zhang, *Adv. Mater.*, 2024, **36**, 2400642.
4 X. Liu, Y. Wang, Z. Wang, S. Zhao, N. Ju, Y. Wang, W. Zhang and H. Sun, *J. Energy Storage*, 2024, **101**, 113798.
5 H. Wang, J. Yang, Y. Cui, J. He, J. Yang, L. Hu, M. Shi and C. Yan, *Chem. Eng. J.*, 2024, **499**, 156034.
6 H. L. Chen and P. Yang, *Chin. J. Chem.*, 2002, **20**, 1529–1535.
7 H. Wu, T. Sun, K. Li, B. Liu, F. Kou, F. Jia, J. Yuan and Y. Bai, *Bioinorg. Chem. Appl.*, 2012, **2012**, 609796.
8 R. Zayani, A. Rabti, S. Ben Aoun and N. Raouafi, *Sens. Actuators, B*, 2021, **327**, 128950.
9 M. Krishnaiah, N. R. de Almeida, V. Udumula, Z. Song, Y. S. Chhonker, M. M. Abdelmoaty, V. A. do Nascimento, D. J. Murry and M. Conda-Sheridan, *Eur. J. Med. Chem.*, 2018, **143**, 936–947.
10 R. W. Huigens, B. R. Brummel, S. Tenneti, A. T. Garrison and T. Xiao, *Molecules*, 2022, **27**, 1112.
11 B. Serafim, A. R. Bernardino, F. Freitas and C. A. V. Torres, *Molecules*, 2023, **28**, 1368.
12 S. H. Lee, D. S. Choi, S. K. Kuk and C. B. Park, *Angew. Chem., Int. Ed.*, 2018, **57**, 7958–7985.
13 R. Chapman and M. H. Stenzel, *J. Am. Chem. Soc.*, 2019, **141**, 2754–2769.
14 S. J. Cobb, A. M. Dharani, A. R. Oliveira, I. A. C. Pereira and E. Reisner, *Angew. Chem., Int. Ed.*, 2023, **62**, e202218782.
15 L. Song, Y. Meng, T. Zhao, L. Liu, X. Pan, B. Huang, H. Yao, R. Lin and R. Tong, *Green Chem.*, 2024, **26**, 428–438.
16 S. Shoda, H. Uyama, J. Kadokawa, S. Kimura and S. Kobayashi, *Chem. Rev.*, 2016, **116**, 2307–2413.
17 T. A. Ngo, E. Nakata, M. Saimura and T. Morii, *J. Am. Chem. Soc.*, 2016, **138**, 3012–3021.
18 Y. H. Shao, Y. D. Gao, Z. L. He and L. C. Yang, *Chem. Catal.*, 2024, **4**, 101068.
19 K. Jiao, G. Sun and S. Zhang, *Sci. China, Ser. B:Chem.*, 1998, **41**, 345–352.
20 X. Zhu, Y. Ding, S. Li, Y. Jiang and Y. Chen, *Sci. Bull.*, 2024, **69**, 483–491.
21 P. Cao, X. Quan, K. Zhao, S. Chen, H. Yu and J. Niu, *J. Hazard. Mater.*, 2020, **382**, 121102.
22 Z. Yang and J. Wang, *Chem. Eng. J.*, 2022, **450**, 138024.
23 T. Tian, W. Wang, Y. Wang, K. Li, Y. Li, W. Fu and Y. Ding, *Chin. J. Catal.*, 2024, **67**, 176–185.
24 C. Ye, Y. Zhou, H. Li and Y. Shen, *Green Chem.*, 2023, **25**, 3931–3939.
25 S. K. Kuk, K. Gopinath, R. K. Singh, T. D. Kim, Y. Lee, W. S. Choi, J. K. Lee and C. B. Park, *ACS Catal.*, 2019, **9**, 5584–5589.
26 C. Jin, N. Li, E. Lin, X. Chen, T. Wang, Y. Wang, M. Yang, W. Liu, J. Yu, Z. Zhang and Y. Chen, *ACS Catal.*, 2022, **12**, 8259–8268.
27 X. Zhu, X. Fan, H. Lin, S. Li, Q. Zhai, Y. Jiang and Y. Chen, *Adv. Energy Mater.*, 2023, **13**, 2300669.
28 Y. Wang, B. Guo, Z. Chai, M. Gao, Y. Li, Y. Yu and S. Huang, *J. Mater. Chem. A*, 2024, **12**, 18537–18543.

29 S. J. Freakley, S. Kochius, J. van Marwijk, C. Fenner, R. J. Lewis, K. Baldenius, S. S. Marais, D. J. Opperman, S. T. L. Harrison, M. Alcalde, M. S. Smit and G. J. Hutchings, *Nat. Commun.*, 2019, **10**, 4178.
30 X. Zhu, J. Wu, R. Liu, H. Xiang, W. Zhang, Q. Chang, S. Wang, R. Jiang, F. Zhao, Q. Li, L. Huang, L. Yan and Y. Zhao, *ACS Nano*, 2022, **16**, 18849–18862.
31 X. Zhu, X. Liu, Y. Ding, S. Li, Y. Jiang and Y. Chen, *Green Chem.*, 2024, **26**, 6039–6045.
32 A. Buchner, F. Tostevin and U. Gerland, *Phys. Rev. Lett.*, 2013, **110**, 208104.
33 H. Wang, Z. Zhao, Y. Liu, C. Shao, F. Bian and Y. Zhao, *Sci. Adv.*, 2018, **4**, eaat2816.
34 L. Wang, J. Zhang, Y. Zhang, H. Yu, Y. Qu and J. Yu, *Small*, 2022, **18**, 2104561.
35 Y. Zhang, H. Jiang, C. Zhang, Y. Feng, H. Feng, S. Zhu and J. Hu, *J. Mater. Chem. A*, 2024, **12**, 6123–6133.
36 Q. Liu, D. Wu, Y. Zhou, H. Su, R. Wang, C. Zhang, S. Yan, M. Xiao and Z. Zou, *ACS Appl. Mater. Interfaces*, 2014, **6**, 2356–2361.
37 N. Li, P. Zhu, Y. Chen, X. Duan and F. Yu, *Surf. Interfaces*, 2018, **10**, 129–135.
38 L. J. Li, Z. F. Hu, Y. Q. Kang, S. Y. Cao, L. P. Xu, L. Yu, L. Z. Zhang and J. C. Yu, *Nat. Commun.*, 2023, **14**, 1890.
39 N. Ramaswamy, U. Tylus, Q. Jia and S. Mukerjee, *J. Am. Chem. Soc.*, 2013, **135**, 15443–15449.
40 A. Kumar, G. Yasin, R. M. Korai, Y. Slimani, M. F. Ali, M. Tabish, M. T. Nazir and T. A. Nguyen, *Inorg. Chem. Commun.*, 2020, **120**, 108160.
41 J. Hernández-Ruiz, M. B. Arnao, A. N. P. Hiner, F. García-Cánovas and M. Acosta, *Biochem. J.*, 2001, **354**, 107–114.
42 A. N. P. Hiner, J. H. Ruiz, J. N. R. g. López, F. G. a. Cánovas, N. C. Brisset, A. T. Smith, M. B. Arnao and M. Acosta, *J. Biol. Chem.*, 2002, **277**, 26879–26885.
43 B. Valderrama, M. Ayala and R. Vazquez-Duhalt, *Chem. Biol.*, 2002, **9**, 555–565.
44 H. Yuan, R. Cai and Z. Pan, *Anal. Lett.*, 2003, **36**, 277–286.
45 D. J. Li, X. W. Li, Y. X. Xie, X. Q. Cai and G. L. Zou, *Biochemistry*, 2005, **70**, 92–99.
46 L. Mei, L. S. Tai, F. H. Tao, S. Jie and L. Q. Rong, *Res. Chem. Intermed.*, 2012, **38**, 499–505.
47 N. Tyagi and P. Mathur, *Spectrochim. Acta, Part A*, 2012, **96**, 759–767.
48 R. Khattar, A. Yadav and P. Mathur, *Spectrochim. Acta, Part A*, 2015, **142**, 375–381.
49 W. Ye, S. Kou, X. Guo, F. Xie, H. Sun, H. Lu and J. Yang, *Nanoscale*, 2015, **7**, 9558–9562.
50 B. A. Maynard, C. D. Tutson, K. S. Lynn, C. W. Pugh and A. E. V. Gorden, *Tetrahedron Lett.*, 2016, **57**, 472–475.
51 Z. Moradi-Shoeili, *React. Kinet., Mech. Catal.*, 2017, **120**, 323–332.
52 F. Vetr, Z. Moradi-Shoeili and S. Özkar, *Appl. Organomet. Chem.*, 2018, **32**, e4465.
53 M. T. Alula and K. Feke, *J. Cluster Sci.*, 2023, **34**, 613–621.
54 S. Sen, S. Basak, S. Pandit, P. Sarkar, T. W. Kim, N. Ghosh, H. J. Kong, J. S. Ryu, B. Singh, R. Roy, R. Mondal, A. Saha, S. Jeon, S. Bhattacharya, J. Im and G. Biswas, *Sci. Rep.*, 2024, **14**, 29684.
55 P. J. Tarcha, V. P. Chu and D. Whittern, *Anal. Biochem.*, 1987, **165**, 230–233.
56 R. Khattar, A. Yadav and P. Mathur, *Spectrochim. Acta, Part A*, 2015, **142**, 375–381.